FLAPPING FLIGHT FOR BIOMIMETIC ROBOTIC INSECTS - PART I: SYSTEM MODELING

by

Xinyan Deng, Luca Schenato, Wei Chung Wu
and Shankar Sastry

Memorandum No. UCB/ERL M04/35

3 September 2004

FLAPPING FLIGHT FOR BIOMIMETIC ROBOTIC INSECTS - PART I: SYSTEM MODELING

by

Xinyan Deng, Luca Schenato, Wei Chung Wu
and Shankar Sastry

Memorandum No. UCB/ERL M04/35

3 September 2004

ELECTRONICS RESEARCH LABORATORY

College of Engineering
University of California, Berkeley
94720

Flapping Flight for Biomimetic Robotic Insects Part I: System Modeling

Xinyan Deng, Luca Schenato, Wei Chung Wu, and Shankar Sastry,
Department of Electrical Engineering and Computer Sciences
University of California at Berkeley
{xinyan,lusche,wcwu,sastry}@eecs.berkeley.edu

Abstract—**This paper presents the mathematical modeling of flapping flight for inch-size micro aerial vehicles (MAVs). These vehicles, called Micromechanical Flying Insects (MFIs), are electromechanical devices propelled by a pair of independent flapping wings and are capable of sustained autonomous flight, and therefore mimic real flying insects. In particular, we describe the design and implementation of the Virtual Insect Flight Simulator (VIFS), a software tool intended for modeling true insect flight mechanisms and for testing the flight control algorithms of the MFIs. The VIFS includes models that have several elements which differ greatly from those with either larger rotary, or fixed wing MAVs. In particular, the VIFS simulates wing-thorax dynamics, the flapping flight aerodynamics at a low Reynolds number regime, and the biomimetic sensory system consisting of ocelli, halteres, magnetic compass and optical flow sensors. In this paper we present a mathematical description for each of these models based on biological principles and experimental data. All these models are designed in a modular fashion for quick upgrading and they are integrated together to give a realistic simulation for MFI flapping flight. The VIFS is intended to serve as a tool to evaluate the performance of the MFI flight control unit with an accurate low-level modeling of dynamics, actuators, sensors and environment.**

Index Terms—**flapping flight, micro aerial vehicles, biomimetic, modeling, low Reynolds number, flying insects.**

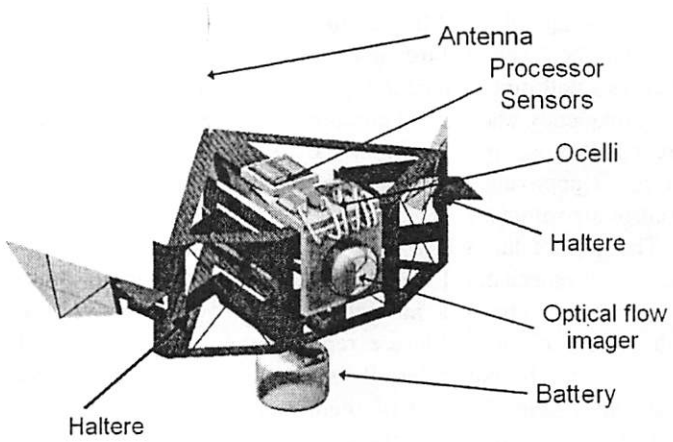

Fig. 1. MFI model based on a blow fly calliphora, with a mass of $100\,mg$, wing length of $11\,mm$, wing beat frequency of $150\,Hz$, and actuator power of $10\,mW$. Each of the wing has two degrees of freedom: flapping and rotation. (Courtesy of R. Fearing and R.J. Wood)

I. Introduction

Micro aerial vehicles (MAVs) have drawn a great deal of interest in the past decade due to the advances in microtechnology. However, most research groups working on MAVs have their designs based on either fixed or rotary wings [1]. It must be noted, though, that fixed and rotary winged MAVs are best suited for outdoor missions, and they have limited applications in urban and highly cluttered environments as a result of their higher speed and bigger size constraints. On the other hand, flapping flying insects, such as fruit flies and house flies, besides being at least two orders of magnitude smaller than today's smallest manmade vehicles, demonstrate superior performance and unmatched maneuverability. These attributes would be beneficial in obstacle avoidance and in navigation in small spaces. Therefore, inspired by true insects, several researchers have started using biomimetic principles to develop MAVs with flapping wings that will be capable of sustained autonomous flight [2], [3], [4]. In particular, the work in this paper has been developed for the Micromechanical Flying Insect (MFI) project at UC Berkeley [5], which has designed a robotic flying insect that mimics a blow-fly. Fig. I shows a conceptual view of the designed robotic fly.

Recently, considerable effort has been directed toward understanding the complex structure of insect flapping flight by examining its components, particularly its sensors [6], [7], [8], [9], the neural processing of external information [10], [11], the biomechanical structure of the wing-thorax system [12], [13], the wing aerodynamics [14], [15], the flight control algorithms [16], and the trajectory planning [17], [18]. However, still little is known about how these elements interact with one another to give rise to the complex behaviors observed in true insects. Therefore, in order to accurately simulate robotic flying insects, we have developed mathematical models for each of the following systems: wing aerodynamics, body dynamics, actuator dynamics, sensors, external environment and flight control algorithms. These models have been integrated together into a single simulator, called the Virtual Insect Flight Simulator (VIFS), aimed both at giving a realistic analysis and at improving the design of sensorial information fusion and flight control algorithms. The mathematical models are based

This work was funded by ONR MURI N00014-98-1-0671,ONR DURIP N00014-99-1-0720 and DARPA.

Authors are with the Robotics and Intelligent Machines Lab at University of California at Berkeley

on today's best understanding of true insect flight, which is far from being complete.

This paper is organized as follows. In Section II we give a brief overview of the MFI project. In Section III we present the modular architecture of VIFS. Sections IV through VII describe in detail respectively the mathematical modelling of flapping flight in a low Reynolds number regime, the insect body dynamics, the wing-thorax actuator dynamics, and the sensory system represented by the ocelli, the halteres, the magnetic compass and the optical flow sensors. Finally, in Section VIII, we state our conclusions and give direction for future work.

II. MFI Overview

The design of the MFI is guided by the studies of true flying insect. The requirements for a successful fabrication, such as small dimensions, low power consumption, high flapping frequency, and limited computational on-board resources, are challenging, however, and they forced the development of novel approaches to electromechanical design and flight control algorithms.

The goal of the MFI project is the fabrication of an inch-size electromechanical device capable of autonomous flight and complex behaviors, mimicking a blowfly Calliphora. The fabrication of such a device requires the design of several components. In particular, it is necessary to identify five main units (Fig. 2), each of them responsible for a distinct task: the *locomotory unit*, the *sensory system unit*, the *power supply unit*, the *communication unit* and the *control unit*. The

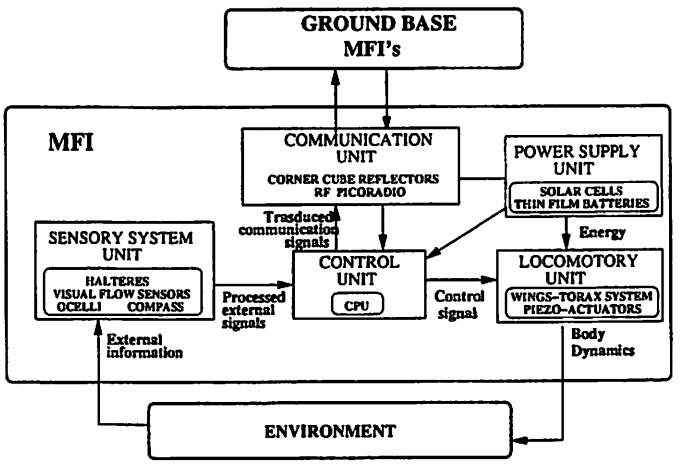

Fig. 2. MFI structure

locomotory unit, composed of the electromechanical thorax-wings system, is responsible for generating the necessary wing motion for the flight, and thus for the MFI dynamics. One of the most challenging parts of this project is the design of a mechanical structure that provides sufficient mobility to the wings to generate the desired wings kinematics. We do not consider these issues in this paper and we direct the interested reader to more detailed work in [19] [20] and references therein. At present, the current design provides two independent wings with two degrees of freedom: flapping and rotation.

The sensory system unit is made up of different sensors. The halteres are biomimetic gyros for angular velocity detection. The ocelli are biomimetic photosensitive devices for roll-pitch estimation and horizon detection. The magnetic compass is used for heading estimation. The optical flow detectors are utilized for self-motion detection and object avoidance. These sensors provide the control unit with the input information necessary to stabilize the flight and to navigate the environment. Other kinds of miniaturized sensors can be installed, such as temperature and chemical sensors, which can be used for search and recognition of particular objects or hazardous chemicals.

The power supply unit, which consists of three thin sheets of solar cells at the base of the MFI body, is the source of electric energy necessary to power the wing actuators and the electronics of all the units. One sheet of solar cells can generate up to $20mWcm^{-1}$. Underneath the solar cell, thin films of batteries can store energy for dim-lit or night condition operation.

The communication unit, based on micro Corner Cube Reflectors (CCR) [21] (a novel optoelectronic transmitter) or on ultra-low-power RF transmitters, provides a MFI with the possibility to communicate with a ground base or with other MFIs.

Finally, the control unit, embedded in the MFI computational circuitry, is responsible both for stabilizing the flight and for planning the appropriate trajectory for each desired task.

III. System Modeling Architecture

In accordance with the major design units of MFI, the VIFS is decomposed into several modular units, each of them responsible for modeling a specific aspect of flapping flight, as shown in Fig. 3.

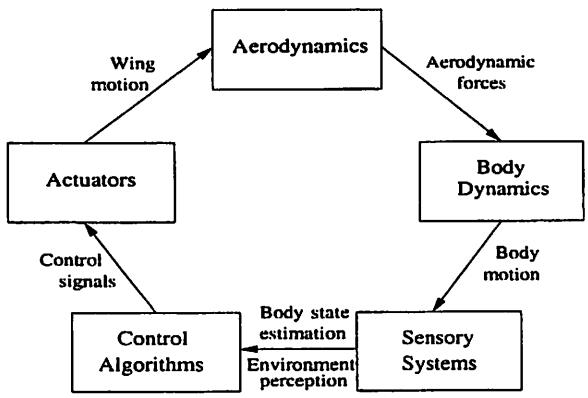

Fig. 3. Simulator (VIFS) architecture

The *Aerodynamic Module* takes as input the wing motion and the MFI body velocities, and gives as output the corresponding aerodynamic forces and torques. This module includes a mathematical model for the aerodynamics, which is described in the next section.

The *Body Dynamics Module* takes the aerodynamics forces and torques generated by the wing kinematics and integrates them along with the dynamical model of the MFI body, thus

computing the body's position and the attitude as a function of time.

The *Sensory System Module* models the sensors used by the MFI to stabilize flight and to navigate the environment. It includes the halteres, the ocelli, the magnetic compass, and optical flow sensors. This module will also include a model for simple environments, *i.e.* a description of the terrain and the objects in it. It takes as input the MFI body dynamics and generates the corresponding sensory information which is used to estimate the MFI's state, i.e. its position and orientation.

The *Control Systems Module* takes as input the signals from the different sensors. Its task is to process the signals and to use that information to generate the necessary control signals to the electromechanical wings-thorax system to stabilize flight and navigate the environment.

The *Actuator Dynamics Module* takes as input the electrical control signals generated by the Control System Module and generates the corresponding wing kinematics. It consists of the model of the electromechanical wings-thorax architecture and the aerodynamic damping on the wings.

The VIFS architecture is extremely flexible since it allows ready modifications or improvements of one single module without rewriting the whole simulator. For example, different combinations of control algorithms and electromechanical structures can be tested, giving rise to the more realistic setting of flight control with limited kinematics due to electromechanical constraints. Moreover, dimensions and masses of the wings and body can be modified to analyze their effects on flight stability, power efficiency and maneuverability. Finally, as better flapping flight aerodynamic models become available, the aerodynamic module can be updated to improve accuracy. The following sections present a detailed mathematical description for the different modules, including simulations and comparisons with experimental results.

IV. Aerodynamics

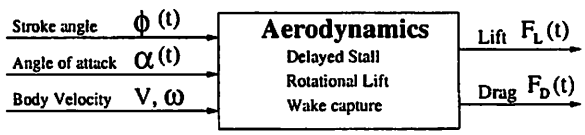

Fig. 4. Block diagram of the Aerodynamical Module

Insect flight aerodynamics, which belongs to the regime of Reynolds number between 30 – 1000, has been a very active area of research in the past decades after the seminal work of Ellington [22]. Although, at present, some numerical simulations of unsteady insect flight aerodynamics based on the finite element solution of the Navier-Stokes equations give accurate results for the estimated aerodynamics forces [23] [24], their implementation is unsuitable for control purposes since they require several hours of processing for simulating a single wingbeat, even on multiprocessor computers. However, several advances have been achieved in comprehending qualitatively and quantitatively unsteady-state aerodynamic mechanisms thanks to scaled models of flapping wings [14], [25]. In particular, the apparatus developed by Dickinson and his group, known as Robofly [14], consists of a two $25cm$-long wings system that mimics the wing motion of flying insects. It is equipped with force sensors at the wing base, which can measure instantaneous wing forces along a wingbeat.

Results obtained with this apparatus have identified three main aerodynamics mechanisms peculiar only to the unsteady state nature of flapping flight: *delayed stall*, *rotational lift* and *wake capture*.

The delayed stall is the result of the translational motion of the wing that starts from rest, and it depends only on the wing translational velocity and angle of attack. It accounts for most of the aerodynamic force generation in flapping flight. This mechanism is unique to flapping flight since it produces large aerodynamic forces for large angles of attack only during the onset of motion and lasts for a distance of a few wing chord lengths. After travelling this distance, turbulent aerodynamic vortices develop behind the wing profile which cause the wing to stall, from which the mechanism takes the name of "delayed" stall. This mechanism can be observed on toy paper airplanes when they are launched from rest: initially they tend to climb because of the large lift generated by the delayed stall, but soon after they fall. Fixed and rotary aircraft cannot exploit this mechanism since they move at a constant velocity and turbulent aerodynamics would arise for large angles of attack.

The second mechanism is the rotational lift that results from the interaction of translational and rotational velocity of the wing at the end of a half-stroke when the wing decelerates and rotates. It is analogous to the effect of back or top spin on a translating tennis ball or baseball, which induces a curved trajectory. However, the fact that the wing profile is flat and not spherical, is an important difference, since the force direction is always perpendicular to wing surface, rather than perpendicular to the velocity vector as in the tennis ball.

Finally, the wake capture is the result of the interaction of the wing with the fluid wake generated in the previous stroke, when the wing inverts its motion. In fact, the fluid behind the wing tends to maintain its velocity due to its inertia, therefore when the wing changes direction, the relative velocity between the wing and the fluid is larger than the absolute wing velocity, thus giving rise to larger force production at the beginning of each half-stroke.

The mathematical aerodynamic modeling presented below is a combination of an analytical model, based on quasi-steady state equations for the delayed stall and rotational lift, and an empirically matched model for the estimation of the aerodynamic coefficients based on experimental data. Wake capture is very complex to treat analytically, and it has not been considered in this work. However, this mechanism is observed to have a small contribution for sinusoidal-like motion of the wings, motion that it is widely used in our simulations and flight control algorithms [26].

A quasi-steady state aerodynamic model assumes that the force equations derived for 2D thin aerofoils translating with constant velocity and constant angle of attack, can be applied also to time varying 3D flapping wings. It is well known from aerodynamics theory [27] that, in steady state conditions, the aerodynamic force per unit length exerted on a aerofoil due

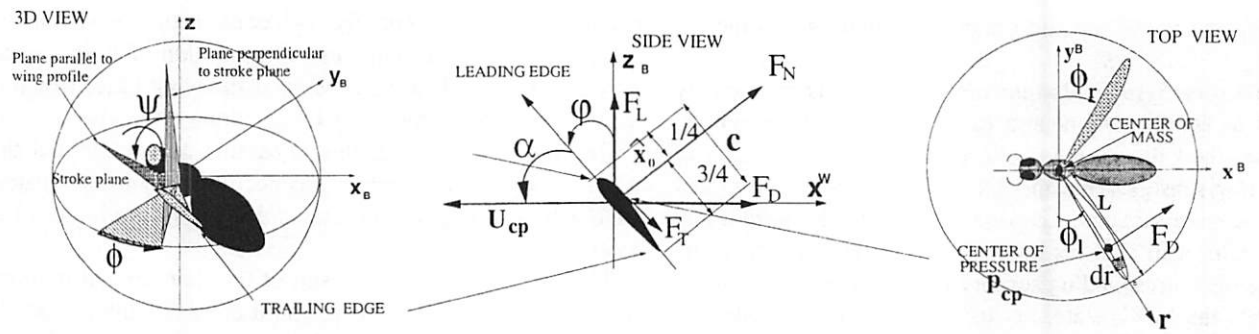

Fig. 5. Definition of wing kinematic parameters: (*left*) 3D view of left wing, (*center*) side view of wing perpendicular to wing axis of rotation $\vec{r}$, (*right*) top view of insect stroke plane

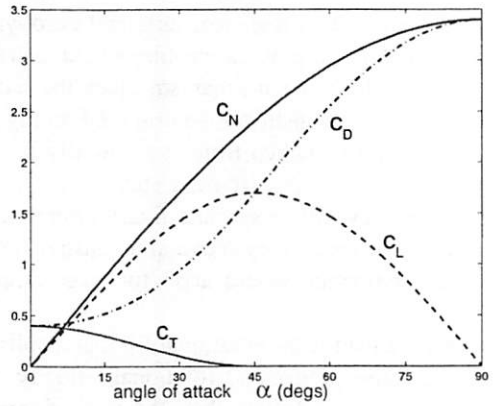

Fig. 6. Aerodynamic force coefficients empirically matched to experimental data [14].

to delayed stall is given by:

$$\begin{aligned} F'_{tr,N} &= \frac{1}{2} C_N(\alpha) \rho c U^2 \\ F'_{tr,T} &= \frac{1}{2} C_T(\alpha) \rho c U^2 \end{aligned} \tag{1}$$

where $F'_{tr,N}$ and $F'_{tr,T}$ are, respectively, the normal and tangential components of the force with respect to the aerofoil profile, c is the cord width of the aerofoil, ρ is the density of air, α is the angle of attack defined as the angle between the wing profile and the wing velocity relative to the fluid, U, and C_N and C_T are the dimensionless force coefficients. The orientation of these forces is always opposite to the wing velocity. Fig. 5 shows a graphical representation of these parameters. A good empirical approximation for the force coefficients is given by:

$$\begin{aligned} C_N(\alpha) &= 3.4 \sin \alpha \\ C_T(\alpha) &= \begin{cases} 0.4 \cos^2(2\alpha) & 0 \le \alpha \le 45^o \\ 0 & \text{otherwise} \end{cases} \end{aligned} \tag{2}$$

which were derived using experimental results given in [14]. These coefficients have been obtained from Equations (1) by experimentally measuring aerodynamic forces for different angles of attack and translational velocities and then solving for the aerodynamic coefficients. Fig. 6 shows the plots of Equations (2). It is clear how, for high angles of attack, the tangential component, mainly due to skin friction, gives only a minor contribution.

In the aerodynamics literature, it is more common to find the lift and drag force coefficients, C_L and C_D. Lift, F_L and drag, F_D are defined, respectively, as the normal and tangential components of the total aerodynamic force with respect to the stroke plane, i.e. the plane of motion of the wings with respect to the body (see Fig. 5a). However, the force decomposition in normal and tangential components is more intuitive, since aerodynamic forces are mainly a pressure force which acts perpendicularly to the surface. Nevertheless, the lift and drag coefficients can be readily computed as:

$$\begin{aligned} C_L(\alpha) &= C_N(\alpha) \cos \alpha - C_T(\alpha) \sin \alpha \\ C_D(\alpha) &= C_N(\alpha) \sin \alpha + C_T(\alpha) \cos \alpha \end{aligned} \tag{3}$$

and they are plotted in Fig. 6. Note how the maximum lift coefficient is achieved for angles of attack of approximately 45^o, considerably different from fixed and rotary wings which produce maximum lift for angles of about 5^o.

The aerodynamic force per unit length exerted on a aerofoil due to rotational lift is given by [28]:

$$F'_{rot,N} = \frac{1}{2} C_{rot} \rho \, c^2 \, U \, \omega \tag{4}$$

where $C_{rot} = 2\pi \left(\frac{3}{4} - \hat{x}_o \right)$ is the rotational force coefficient, approximately independent of the angle of attack, $\hat{x}_o$ is the dimensionless distance of the longitudinal rotation axis from the leading edge, and ω is the angular velocity of the wing with respect to that axis. In most flying insects $\hat{x}_o$ is about $\frac{1}{4}$, which correspond to the theoretical value of the mean center of pressure along the wing chord direction. This is a pure pressure force and therefore acts perpendicularly to the wing profile, in the opposite direction of wing velocity.

According to the quasi-steady state approach, the total force on a wing is computed by dividing the wing into infinitesimal blades of thickness dr, as shown in Fig. 5(c). First, we calculate the total force on each blade:

$$\begin{aligned} dF_{tr,N}(t,r) &= \frac{1}{2} C_N(\alpha(t)) \rho \, c(r) \, U^2(t,r) \, dr \\ dF_{tr,T}(t,r) &= \frac{1}{2} C_T(\alpha(t)) \rho \, c(r) \, U^2(t,r) \, dr \\ dF_{rot,N}(t) &= \frac{1}{2} C_{rot} \rho \, c(r)^2 \, U(t,r) \, \dot{\alpha}(t) \, dr \\ U(t,r) &= \dot{\phi}(t) r \end{aligned} \tag{5}$$

where ϕ is the stroke angle, and the wing angular velocity, ω is approximately $\dot{\alpha}$. Then we integrate the forces in Equations (5) along the wing, i.e. $F_{tr,N}(t) = \int_0^L dF_{tr,N}(t,r)$, to get:

$$F_{tr,N}(t) = \frac{1}{2}\rho A_w C_N(\alpha(t)) U_{cp}^2(t) \quad (6)$$

$$F_{tr,T}(t) = \frac{1}{2}\rho A_w C_T(\alpha(t)) U_{cp}^2(t) \quad (7)$$

$$F_{rot,N}(t) = \frac{1}{2}\rho A_w C_{rot}\, \hat{c}\, c_m\, \dot{\alpha}(t) U_{cp}(t) \quad (8)$$

$$U_{cp}(t) = \hat{r}_2 L \dot{\phi}(t) \quad (9)$$

where A_w is the wing area, L is the wing length, U_{cp} is the velocity of the wing at the center of pressure, $\hat{r}_2$ is the normalized center of pressure, c_m is maximum wing chord width, and $\hat{c}$ is the normalized rotational chord. The former two parameters are defined as follows:

$$\hat{r}_2^2 = \frac{\int_0^L c(r)\, r^2\, dr}{L^2 A_w}$$

$$\hat{c} = \frac{\int_0^L c^2(r)\, r\, dr}{\hat{r}_2 L A_w c_m}$$

The normalized center of pressure, $\hat{r}_2$, and the normalized rotational chord, $\hat{c}$, depend only on the wing morphology, and in most flying insects their range is approximately $\hat{r}_2 = 0.6 - 0.7$ and $\hat{c} = 0.5 - 0.75$ [22]. As a result of this approach, the wing forces can be assumed to be applied at a distance, $p_{cp} = \hat{r}_2 L$, from the wing base. According to thin aerofoil theory, the center of pressure r_{cp} lies about $\frac{1}{4}$ of chord length from the leading edge (see Fig. 5(b)). This has been confirmed by numerical simulations of insect flight which do not assume a quasi-steady state aerodynamic regime [23], and by experiments performed with a scaled model of insect wings [14].

If the velocity of the insect body is comparable with the mean wing velocity of the center of pressure, as during cruising flight, a more accurate model for estimating the aerodynamic forces is based on finding the absolute velocity of the center of pressure of the wing relative to an inertial frame, which is obtained by substituting Equation (9) with the following:

$$U_{cp}(t) = \hat{r}_2 L \dot{\phi}(t) + v^b(t) \quad (10)$$

where $v^b(t)$ is the velocity of the insect body relative to the inertial frame represented in the wing frame coordinate system. The total lift and drag forces acting on the wing can be derived through a trigonometric transformation analogous to the one used in Equations (3) as follows:

$$\begin{aligned} F_N(t) &= F_{tr,N}(t) + F_{rot,N}(t) \\ F_T(t) &= F_{tr,T}(t) \\ F_D(t) &= F_N(t)\cos\alpha(t) - F_T(t)\sin\alpha(t) \\ F_L(t) &= F_N(t)\sin\alpha(t) + F_T(t)\cos\alpha(t) \end{aligned} \quad (11)$$

where $F_{tr,N}, F_{tr,T}, F_{rot,N}$ are given in Equations (6),(7), and (8), respectively, and $U_{cp}(t)$ is given in Equation (10).

The aerodynamic forces used for simulation are based on Equations (11). Fig. 7 shows the simulated aerodynamic forces for a typical wing motion and the corresponding experimental results obtained with a dynamically scaled model of insect wing (Robofly traces). Despite some small discrepancies due to the undermodeling of the wake capture mechanism, our mathematical model predicts the experimental data sufficiently well .

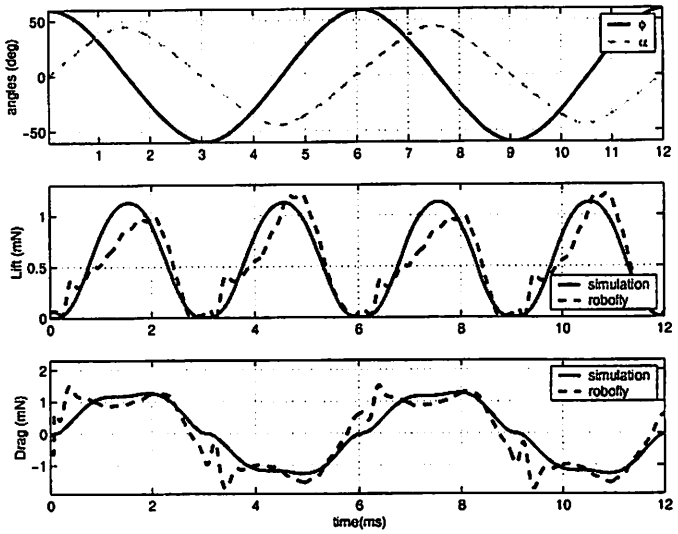

Fig. 7. From top to bottom: stroke(solid) and rotation(dashed) angles, lift and drag forces (solid) calculated from Equation (11) compared with experimental data (dashed) from the Robofly during the course of two wingbeats (Robofly data are courtesy of M. H. Dickinson).

The flapping flight aerodynamics module implementation is summarized in the block diagram of Fig. 4.

V. Body Dynamics

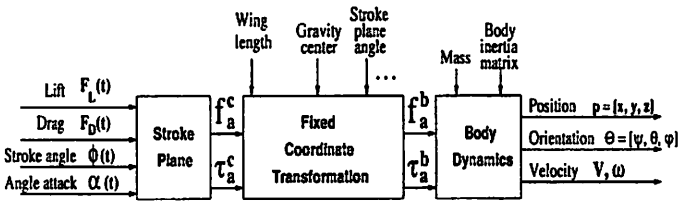

Fig. 8. Body Dynamics Block Diagram

The body dynamic equations compute the evolution of the dynamics of the insect center of mass and insect orientation with respect to an inertial frame. This evolution is the result of the wings' inertial forces, and the external forces, specifically aerodynamic forces, body damping forces, and the force of gravity. However, the mass of the wings is only a small percent of the insect body mass and as they move almost symmetrically, their effect on insect body dynamics is likely to cancel out within a single wingbeat. In fact, even if wing inertial forces are larger than aerodynamic forces, nonholonomic rotations would be possible for frictionless robots with moving links (see [29] Example 7.2) only if the links, in our case the wings, would flap out of sync with each other, an activity not observed in true insects. Therefore, based on this observation, it seems safe to assume that one can disregard inertial forces and simplify the evolution of the insect dynamics to a single rigid body under the effect of external forces only.

As shown in [29], the equations for rigid body motion subject to an external wrench $F^b = [f^b, \tau^b]^T$ applied at

the center of mass and specified with respect to the body coordinate frame, are given as:

$$\begin{bmatrix} \mathrm{mI} & 0 \\ 0 & \mathcal{I} \end{bmatrix} \begin{bmatrix} \dot{v}^b \\ \dot{\omega}^b \end{bmatrix} + \begin{bmatrix} \omega^b \times mv^b \\ \omega^b \times \mathcal{I}\omega^b \end{bmatrix} = \begin{bmatrix} f^b \\ \tau^b \end{bmatrix} \quad (12)$$

where m is the mass of the insect, $\mathcal{I}$ is the insect body inertia matrix relative to the center of mass, v^b is the velocity vector of the center of mass in body frame coordinates, and ω^b is the angular velocity vector in body frame coordinates. The values for the body and wing morphological parameters, such as lengths and masses, used in our simulations are those of a typical blowfly. However, they can be changed thus allowing the simulation of different species and MFI designs.

The total forces and torques in the body frame are given by the sum of the three external forces, i.e. the aerodynamic forces, f_a^b, the body damping forces, f_d^b, and the gravity force, f_g^b:

$$\begin{aligned} f^b &= f_a^b + f_g^b + f_d^b \\ \tau^b &= \tau_a^b + \tau_g^b + \tau_d^b \end{aligned} \quad (13)$$

The aerodynamic forces and torques relative to the insect center of mass, can be obtained by a sequence of fixed coordinate transformations, starting from lift and drag forces and wings kinematics calculated by the aerodynamic module as follows:

$$\begin{aligned} f_a^b(t) &= f_a^l(t) + f_a^r(t) \\ \tau_a^b(t) &= p_l(t) \times f_a^l(t) + p_r(t) \times f_a^r(t) \end{aligned} \quad (14)$$

where the subscripts l, r stand for left and right wing, respectively, and $p(t)$ is the position vector of the center of pressure of the wing relative to the body center of mass.

Since the lift and drag forces given by Equations (11) are calculated relative to the *stroke plane frame*, a coordinate transformation is necessary before obtaining the forces and torques acting on the *body frame*. The *insect body frame* is defined as the coordinate system attached to the body center of gravity and with x-axis oriented from tail to head, the y-axis from right wing hinge to left wing hinge, and the z-axis from ventral to dorsal side of the abdomen. Since these are the axes of symmetry of the insect, the matrix of inertia is almost diagonal in the body frame. The *stroke plane frame* is the coordinate system attached to the center of the thorax at the center of the wings base, whose x-y plane is defined as the plane to which the wing motion is approximately confined during flapping flight.

Given the lift and drag generated by aerodynamics, together with the stroke angle, the forces and torques in the *stroke plane* can be calculated as

$$f_a^c = \begin{bmatrix} F_D^l \cos\phi_l + F_D^r \cos\phi_r \\ F_D^l \sin\phi_l - F_D^r \sin\phi_r \\ F_L^l + F_L^r \end{bmatrix}$$

$$\tau_a^c = \hat{r}_2 L \begin{bmatrix} -F_D^l \cos\phi_l + F_L^r \cos\phi_r \\ -F_D^l \sin\phi_l - F_D^r \sin\phi_r \\ F_D^l - F_D^r \end{bmatrix}$$

where we used $p_l(t) = \hat{r}_2 L(\sin\phi_l, \cos\phi_l, 0)$ and $p_r(t) = \hat{r}_2 L(\sin\phi_r, \cos\phi_r, 0)$. To obtain the aerodynamics forces and torques in the *body frame*, we do a coordinate transformation as:

$$\begin{bmatrix} f_a^b \\ \tau_a^b \end{bmatrix} = \begin{bmatrix} R_{cb}^T & 0 \\ -R_{cb}^T \hat{p_{cb}} & R_{cb}^T \end{bmatrix} \begin{bmatrix} f_a^c \\ \tau_a^c \end{bmatrix} \quad (15)$$

where R_{cb} is the rotation matrix of the body frame relative to the stroke plane, and p_{cb} represents the translation of the origin of the body frame from the stroke plane. This is a fixed transformation that depends only on the morphology of the insect or MFI.

The gravitational forces and torques in the *body frame* are given by:

$$\begin{bmatrix} f_g^b \\ \tau_g^b \end{bmatrix} = \begin{bmatrix} R^T \begin{bmatrix} 0 \\ 0 \\ mg \end{bmatrix} \\ 0 \end{bmatrix} \quad (16)$$

where R is the rotational matrix of the body frame relative to the spatial frame, and g is the gravitational acceleration.

The viscous damping exerted by the air on the insect body is approximately given by:

$$\begin{bmatrix} f_d^b \\ \tau_d^b \end{bmatrix} = \begin{bmatrix} -bv^b \\ 0 \end{bmatrix} \quad (17)$$

where b is the viscous damping coefficient. The reason for the linearity in the velocity of the drag force is that the velocity of the insect is small relative to insect size, therefore viscous damping prevails over quadratic inertial drag. Empirical evidence for linear damping has been recently observed by the authors by analyzing the free flight dynamics of true fruit flies. Moreover, theoretic computations [30] and experimental data [31] indicate that rotational damping of the insect body is negligible relative to aerodynamic forces even during rapid body rotation and can therefore be neglected.

Numerical solution of Equations (12) have been implemented using Euler's angle representation for the rotation matrix. This representation is very commonly used in space vehicle dynamics modeling and the notation that follows can be found in many textbooks such as [32]. In particular, we consider the new variables $\dot{P} = v^p = Rv^b$ and $\hat{\omega}^b = R^T\dot{R}$. For $R \in SO(3)$, we parametrize R by ZYX Euler's angles with φ, θ, and ψ about x,y,z axes respectively, and hence $R = e^{\hat{z}\psi}e^{\hat{y}\theta}e^{\hat{x}\varphi}$ with $x = [1\ 0\ 0]^T$, $y = [1\ 0\ 0]^T$,$z = [0\ 0\ 1]^T$ and $\hat{x}, \hat{y}, \hat{z} \in so(3)$. By differentiating R with respect to time, we have the state equations of the Euler angles, $\Theta = [\varphi\ \theta\ \psi]^T$, which can be defined as $\dot{\Theta} = W\omega^b$. By defining the state vector $[P, \Theta] \in \mathbb{R}^3 \times \mathbb{R}^3$ where P is the position of the center of mass w.r.t. the inertia frame, and Θ are the euler angles which we use to parametrize the rotation matrix R, we can rewrite the equations of motion of a rigid body as:

$$\begin{aligned} \ddot{\Theta} &= (\mathcal{I}W)^{-1}[\tau^b - W\dot{\Theta} \times \mathcal{I}W\dot{\Theta} - \mathcal{I}\dot{W}\dot{\Theta}] \\ \ddot{P} &= \frac{1}{m}Rf^b \end{aligned} \quad (18)$$

where the body forces and torques (f^b, τ^b) are time-varying, nonlinear functions of the wing kinematics and body orientation and are given by Equations (13).

The body dynamic module implementation is summarized in the block diagram in Fig. 8.

VI. Actuator Dynamics

Each wing is moved by the thorax, a complex trapezoidal structure actuated by two piezoelectric actuators at its base, as

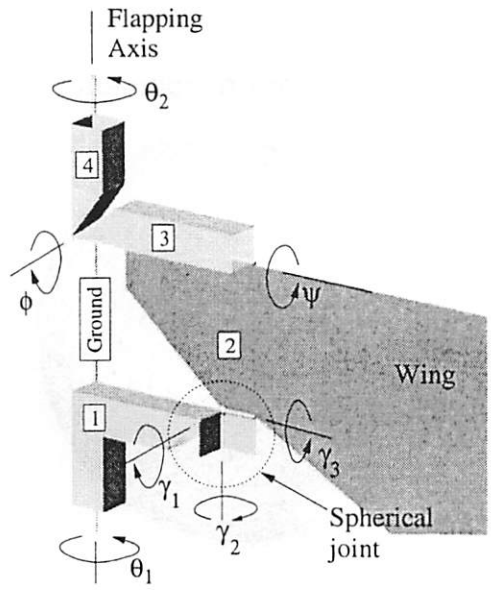

Fig. 9. Wing-Thorax structure. Courtesy of [33]

shown in Fig. 9. A complete nonlinear model for the thorax, developed in [33], can be written as follows

$$M\begin{bmatrix}\ddot{\theta}_2\\ \ddot{\beta}\end{bmatrix}+B\begin{bmatrix}\dot{\theta}_2\\ \dot{\beta}\end{bmatrix}+K\begin{bmatrix}\theta_2\\ \beta\end{bmatrix}+\begin{bmatrix}0\\ f(\dot{\beta})\end{bmatrix}=T\begin{bmatrix}u_1\\ u_2\end{bmatrix} \quad (19)$$

where $f(\dot{\beta}) = \frac{1}{2}m'_{\omega,2}(\dot{\beta})^2$, θ_2 is the leading edge flapping angle from the four bar mechanism, $\beta = \theta_1 - \theta_2$ is the phase difference between the four bar output angles, u_1 and u_2 are the control input torques to the actuators, M and B are the inertia and damping matrices, which are assumed to be constant. However, parameters in K and T matrices include some slowly time varying terms, and the control inputs (u_1, u_2) are limited to $10\mu Nm$ by physical constraints.

The relationship between the state variables in Equation (19) and the wing motion variables (stroke angle ϕ and rotation angle φ, see Fig. 5) can be approximated as $\phi = \theta_2$ and $\varphi = 2\beta$. Based on Equation (19), with a change of variables, neglecting the nonlinear components, we can derive the linear actuator model as

$$M_0\begin{bmatrix}\ddot{\phi}\\ \ddot{\varphi}\end{bmatrix}+B_0\begin{bmatrix}\dot{\phi}\\ \dot{\varphi}\end{bmatrix}+K_0\begin{bmatrix}\phi\\ \varphi\end{bmatrix}=T_0\begin{bmatrix}u_1\\ u_2\end{bmatrix} \quad (20)$$

where M_0, B_0, K_0, and T_0 are constant matrices calculated from the data provided in [33].

Equation (20) is a stable linear MIMO system and can also be written using a transfer function representation in the frequency domain:

$$Y(j\omega) = G(j\omega)U(j\omega)$$

where Y and U are the Fourier transform of the output vector $y = (\phi, \varphi)$ and the input vector $u = (u_1, u_2)$, respectively. The electromechanical structure has been designed so that the input-output frequency response of the system is almost decoupled at all frequencies, i.e. $|G_{11}(j\omega)| \simeq |G_{22}(j\omega)| \gg |G_{12}(j\omega)| \simeq |G_{21}(j\omega)|, \forall\omega$, where G_{ik} represents the $i-k$ entry of the matrix G, and $\omega = 2\pi f$. Moreover, the system has also been designed to achieve a quality factor $Q = 3$ at the desired resonant frequency of $f_0 = 150Hz$, *i.e.* $|G_{ii}(j2\pi f_0)| \simeq |G_{ii}(0)|$. A low quality factor Q is necessary to easily control the wing trajectory even when the wingbeat frequency is the same as the resonant frequency. In fact, large Qs would practically remove all higher order harmonics from the input signals and the wing would simply oscillate along the same sinusoidal trajectory.

VII. Sensory System

This section briefly describes the sensory systems of the MFI, which include the ocelli, the magnetic compass, the halteres, and the optic flow sensors. The ocelli can be used to estimate the roll and pitch angles, the magnetic compass to estimate the yaw angle, the halteres to estimate the three angular velocities, and the optic flow sensors for object avoidance and navigation.

In this paper we only provide the mathematical modeling of these sensors. Their role in flight stabilization and navigation are presented in [34] and in the references therein. These sensors are currently being implemented, and preliminary results of their prototypes are presented in [35].

A. Ocelli

Ocelli form a sensory system present in many flying insects. This system comprises three wide angle photoreceptors placed on the head of the insect. They are oriented in such a way that they collect light from different regions of the sky. The ocelli are believed to play an important role in attitude stabilization in insect flight as they compare the light intensity measured by the different photoreceptors, which in turn act as horizon detectors [8]. Inspired by the ocelli of true insects, we developed a biomimetic, ocelli-like system composed of four photoreceptors. The light intensity function for a point on the sky sphere $I = I(\alpha, \beta)$ is a function of the latitude, α, and longitude, β, relative to the fixed frame. This modeling is sufficient to realistically describe light intensity distributions for different scenarios, such as indoor, outdoor and urban environments.

The ocelli system is modeled as four ideal photoreceptors, P_1, P_2, P_3, and P_4, fixed with respect to the body frame. They are oriented symmetrically with the same latitude, and, if their axes are drawn, one would see that the axes form a pyramid whose top vertex is located at the center of the insect's head. Every photoreceptor collects light from a conic region A_i in the sky sphere around its ideal orientation P_i as shown in Fig. 10a.

The measurements from the photoreceptors are simply subtracted pairwise and these two signals are the output from the ocelli:

$$y_1^o = I(P_1) - I(P_2), \qquad y_2^o = I(P_3) - I(P_4) \quad (21)$$

where $I(P_i)$ is the output from the i-th photodiode. The orientation of the photodiodes relative to the fixed frame, i.e., the latitude and longitude of the area of sky they are pointing at, is a function of the insect orientation, i.e., $P_i = P_i(R)$, where R is the body orientation matrix. Therefore, if the light

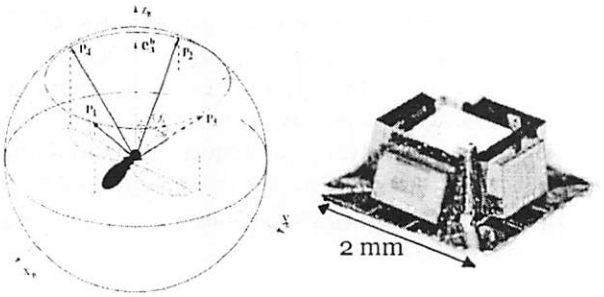

Fig. 10. (a) Graphical rendering of ocelli present in flying insects. Four photoreceptors, P_1, P_2, P_3, and P_4, collect light from different regions of the sky. The shadowed area represents such a region for photoreceptor P_3; (b) Photo of the ocelli sensor prototype.

intensity function, $I = I(\alpha, \beta)$ is defined, given the orientation of the insect body, R, the output of the ocelli can be computed from Equation (21). If the light intensity in the environment is a monotonically decreasing function of its latitude relative to the light source, i.e., $I = I(\alpha)$, then it is shown in [34] that the outputs from the ocelli can be used as an estimate of the orientation of the ocelli reference frame relative to the light source. In fact, for small deviations from the vertical orientation we have $y_1^o \simeq k_o \psi$ and $y_2^o \simeq k_o \theta$, where k_o is a positive constant, and (ψ, θ) are the roll and pitch body angles, respectively. More general theoretical and experimental results for attitude stabilization using ocelli are given in [34]. Even if in real environments light intensity is not exactly a monotonically decreasing function, the ocelli can still estimate robustly the orientation of the body frame relative to the light source, as shown in Fig. 11 where the light intensity function $I(\alpha, \beta)$ was collected using the ocelli prototype shown in Fig. 10b.

B. Magnetic Compass

Although the ocelli system provides a means for a flying insect to reorient its body towards a specific orientation, its heading remains arbitrary. Since maintaining the heading is fundamental for forward flight and maneuvering, we propose to solve this problem by implementing a magnetic compass for the MFI. This magnetic sensor can estimate the heading based on the terrestrial geomagnetic field. The magnetic compass has three "U-shaped" suspended structures as shown in Fig. 12b (see [35] for details). Electric current flows through these loops, interacting with the terrestrial geomagnetic field, and induces the Lorentz force given by $\mathbf{F}_l = 3L\mathbf{i} \times \mathbf{B}$, where $\mathbf{F}_l$ is the total force at the base of the cantilever, $3L$ is the length of one loop of the cantilever, $\mathbf{i}$ is the total current, and $\mathbf{B}$ is the terrestrial geomagnetic field. The deflection of the cantilever, which is proportional to the force perpendicular to the cantilever, i.e., $F_c = \mathbf{F}_l \cdot \mathbf{n}$ where $\mathbf{n}$ is the sensing direction of the strain gauge, is sensed at the base by strain gauges. Thus, the outputs from the strain gauges can be used to estimate the heading of the MFI and it is given by:

$$y^c = aF_c = aL(\mathbf{i} \times \mathbf{B}) \cdot \mathbf{n} = k_c \sin\gamma = k_c f(R) \qquad (22)$$

where a is a constant that depends on the size of the cantilever and the strain gauge, γ is the angle between the insect

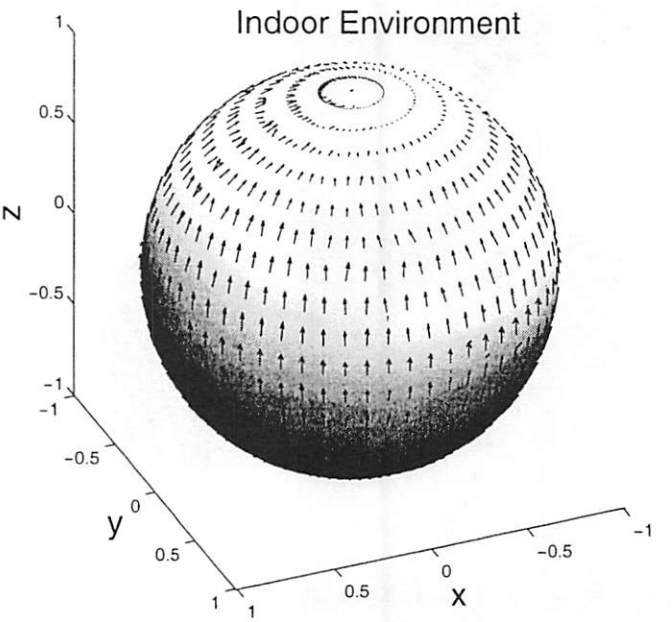

Fig. 11. Light intensity distribution and estimated light source position using experimental data collected from an ocelli prototype [34].

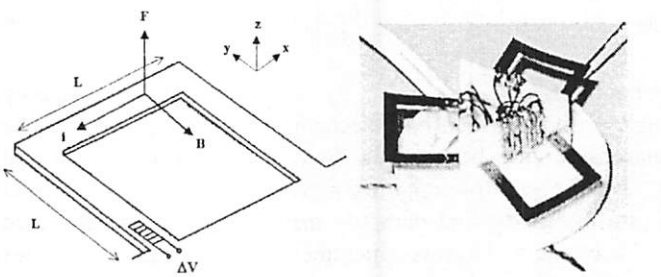

Fig. 12. (a) Schematic of a magnetic compass; (b) Photo of the magnetic sensor prototype. Courtesy of [36].

heading and the direction of the Earth magnetic field, and $f(R)$ is a linear function of the body rotation matrix R. The function $f(R)$ can be computed easily once the orientation of the current vector $\mathbf{i}^b$ and the gauge sensing direction $\mathbf{n}^b$, with respect to body frame, and the orientation of the Earth magnetic field $\mathbf{B}^f$, relative to the fixed frame, are known.

C. Halteres

Biomechanical studies on insect flight revealed that in order to maintain stable flight, insects use structures, called halteres, to measure body rotations via gyroscopic forces [37]. The halteres of a fly resemble small balls at the end of thin sticks as shown in Fig. 13a. During flight the two halteres beat up and down in non-coplanar planes through an angle of nearly 180° anti-phase to the wings at the wingbeat frequency. This non-coplanarity of the two halteres is essential for a fly to detect rotations about all three turning axes because a fly with only one haltere is unable to detect rotations about an axis perpendicular to the stroke plane of that haltere [7].

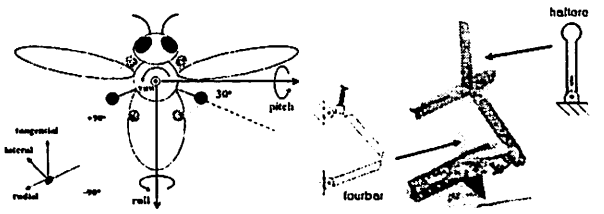

Fig. 13. (a) Schematic of the halteres (enlarged) of a fly; (b) Photo of the haltere prototype. Courtesy of [36].

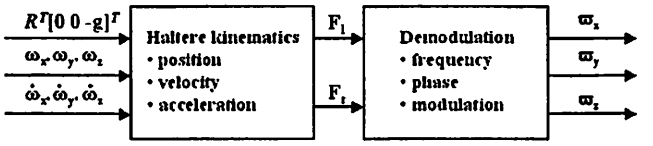

Fig. 14. Block diagram of the haltere process. R is the insect body rotation matrix. Details of the demodulation scheme are presented in [36].

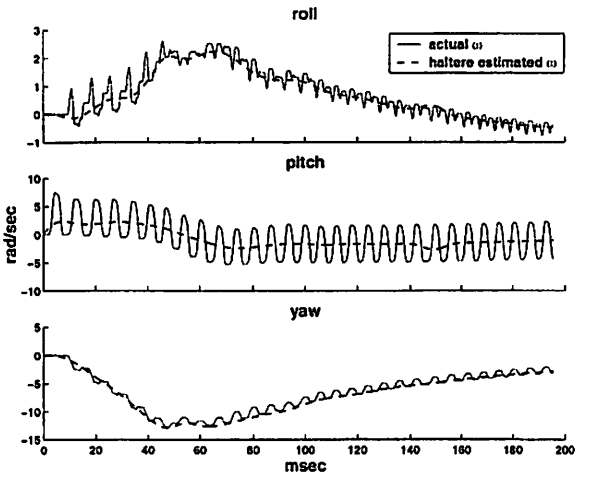

Fig. 15. Simulation of angular velocity detection by halteres under a steering flight mode.

As a result of insect motion and haltere kinematics, a complex set of forces acts on the halteres during flight: gravitational, inertial, angular acceleration, centrifugal, and Coriolis forces.

$$\mathbf{F} = m\mathbf{g} - m\mathbf{a} - m\dot{\omega} \times \mathbf{r} - m\omega \times (\omega \times \mathbf{r}) - 2m\omega \times \mathbf{v} \quad (23)$$

where m is the mass of the haltere, $\mathbf{r}$, $\mathbf{v}$, and $\mathbf{a}$ are the position, velocity, and acceleration of the haltere relative to the insect body, ω and $\dot{\omega}$ are the angular velocity and angular acceleration of the insect, and $\mathbf{g}$ is the gravitational constant (see Fig. 14). However, by taking the advantage of the unique characteristics (frequency, modulation, and phase) of the Coriolis signals on the left and right halteres, a demodulation scheme has been proposed to decipher roll, pitch, and yaw angular velocities from the complex haltere forces [36]. Fig. 15 shows the decoupled angular velocities of a fly estimated by processing the haltere force measurements during a steering flight mode, obtained using simulations of insect flight according to the body dynamics described in the previous section. It is shown in [34] that the haltere outputs are almost equivalent to the following smoothed version of the insect angular velocities:

$$\begin{aligned} y_1^h(t) &= \frac{k_{h1}}{T}\int_{t-T}^{t}\omega_x(\tau)\mathrm{d}\tau = \bar{\omega}_x(t) \\ y_2^h(t) &= \frac{k_{h2}}{T}\int_{t-T}^{t}\omega_y(\tau)\mathrm{d}\tau = \bar{\omega}_y(t) \\ y_3^h(t) &= \frac{k_{h3}}{T}\int_{t-T}^{t}\omega_z(\tau)\mathrm{d}\tau = \bar{\omega}_z(t) \end{aligned} \quad (24)$$

where T is the period of oscillation of the halteres, k_{h1}, k_{h2}, and k_{h3} are positive constants, and $\bar{\omega}_i$ are the mean angular velocities of the insect during one period of oscillation of the halteres. Fig. 13b shows the prototype of the haltere sensor.

D. Optic Flow Sensors

Research on insects' motion-dependent behavior contributed to the characterizations of certain motion-sensing mechanisms in flying insects. The correlation model of motion detection represents the signal transduction pathway in a fly's visual system [38] [39]. The basic element of the Reichardt correction-based motion sensor is an elementary motion detector (EMD),

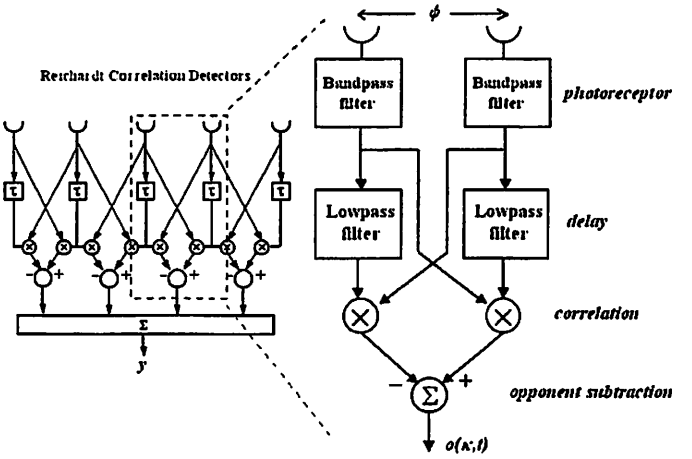

Fig. 16. Elementary motion detector (EMD) architecture.

as shown in Fig. 16. When a moving stimulus is detected by an EMD, the perceived signal in one photoreceptor is compared to the delayed signal in a neighboring photoreceptor. If the signal in the left photoreceptor correlates more strongly to the delayed signal in the right photoreceptor, the stimulus is moving from right to left and vice versa. In the EMD implementation, as in [40], the photoreceptor can be modeled as a bandpass filter whose transfer function is given by

$$P(s) = \frac{K \cdot \tau_H \cdot s}{(\tau_H \cdot s + 1)(\tau_{photo} \cdot s + 1)} \quad (25)$$

where τ_H is the time constant of the DC-blocking highpass filter, τ_{photo} is the time constant defining the bandwidth of the photoreceptor, and K is the constant of proportionality. The delay operation of the EMD can be realized by a lowpass filter with time constant τ:

$$D(s) = \frac{1}{\tau \cdot s + 1} \quad (26)$$

The correlation is achieved by multiplying the delayed signal in one leg of the EMD with the signal in the adjacent

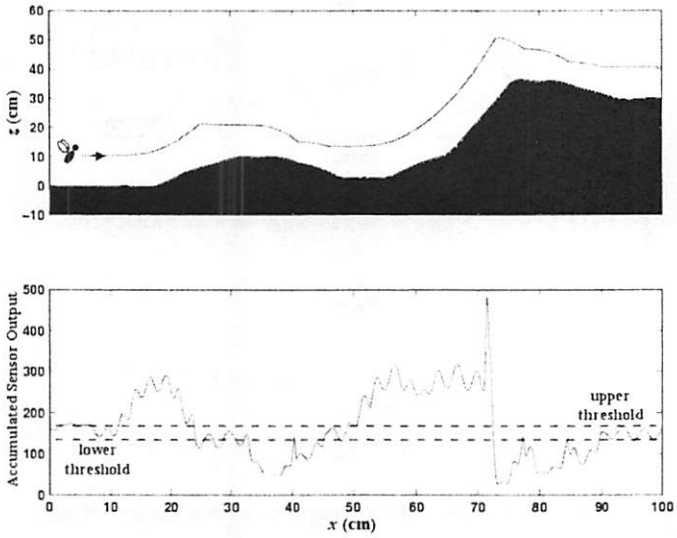

Fig. 17. A fly follows the topography of the ground (top) based on the perceived optic flow (bottom) during the flight.

leg and the signals in the two legs are subtracted, and the detector output is thus the remainder. Finally, the outputs of the individual units in the array are added together to obtain an overall sensor output:

$$y^f(t) = \sum_{\kappa} o(\kappa, t) \tag{27}$$

where κ is the number of EMDs in the array. This spatial summation has the effect of reducing oscillations in the output of a single EMD [41].

Image motions seen by an insect's eyes are encoded by the perceived optic flow. Higher image motions result in greater optic flow. Therefore, when an insect flies toward an object, the quick expansion of that object in the insect's visual field would induce large optic flow across its eyes. This kind of flow signal can be exploited to perform tasks such as obstacle avoidance and terrain following. In the simulation of a fly following a simple topography of the ground (see top panel of Fig. 17), optic flow measurements are estimated by simulating an array of EMDs based on the configuration in Fig. 16, and calculating the signals using Equations (25), (26), and (27) according to the fly's elevation. The flow sensor is assumed to face downward by 60° on the head of the fly. The bottom panel shows the accumulated optic flow perceived by the sensor during the flight. When the fly is closer to the ground, the patterns on the ground cause the optic flow to increase quickly. An upper threshold for the perceived optic flow is set such that when this value is reached, the fly would elevate in order to maintain a safe distance to the ground. On the other hand, when the fly is at a higher position, the patterns on the ground do not induce significant optic flow and hence the flow signals decrease due to leakage over time. Accordingly, the fly would descend when a preset lower threshold is reached. By selecting appropriate upper and lower threshold values, the fly can follow the topography of the ground properly.

VIII. Conclusion

In this paper we presented a mathematical model for flapping flight inch-size micromechanical flying vehicles. The aerodynamics, the elctromechanical architecture, and the sensory system for these vehicles differ considerably from larger rotary and fixed-winged aircrafts, and require specific modeling. Based on latest research developed in the biological community, and the understanding of physical limitations of the actual device, we built a realistic simulation testbed, called Virtual Insect Flight Simulator, which captures the most important features for this kind of flapping wing micro aerial vehicles. Mathematical modeling and simulations have been presented for the aerodynamics, the insect body dynamics, the electromechanical wing-thorax dynamics, the ocelli, the halteres, the magnetic compass, and the optical flow sensors. Comparison between simulations and experimental results have been given, when possible, to validate the modeling. This simulator has been used extensively to test flight control architectures and algorithms, which are presented in a companion paper [26]. The modularity of the implementation is intended to ease the modification of the simulator as better modeling becomes available or additional elements are included in the future, such as a modeling for the wake capture in the aerodynamics module and the compound-eye visual processing for object fixation and recognition in the sensory system.

IX. Acknowledgments

The authors wish to thank R.S. Fearing for his helpful comments, and S. Avadhanula for providing the model for the wing-thorax system. We also want to thank R.J Wood for designing, building, and testing the halteres prototype, and R. Sahai, S. Bergbreiter and B. Leibowitz for designing and fabricating the ocelli prototype.

References

[1] B. Motazed, D. Vos, and M. Drela, "Aerodynamics and flight control design for hovering MAVs," in *Proceedings of American Control Conference*, Philadelphia, PA, June 1998, pp. 681–683.

[2] R.S. Fearing, K.H. Chiang, M.H. Dickinson, D.L. Pick, M. Sitti, and J. Yan, "Wing transmission for a micromechanical flying insect," in *Proceeding of IEEE International Conference on Robotics and Automation*, 2000, pp. 1509–1516.

[3] R.C. Michelson and M.A. Naqvi, "Beyond biologically inspired insect flight," in *von Karman Institute for Fluid Dynamics RTO/AVT Lecture Series on Low Reynolds Number Aerodynamics on Aircraft Including Applications in Emergening UAV Technology*, Brussels, Belgium, 2003, pp. 1–19.

[4] T. Pornsin-Sisirak, S.W. Lee, H. Nassef, J. Grasmeyer, Y.C. Tai, C.M. Ho, and M. Keennon, "MEMS wing technology for a battery-powered ornithopter," in *Thirteenth IEEE International Conference on Micro Electro Mechanical Systems (MEMS '00)*, Miyazaki, Japan, 2000, pp. 799–804.

[5] Micromechanical Flying Insect website, "http://robotics.eecs.berkeley.edu/~ronf/mfi.html," .

[6] W.P. Chan, F. Prete, and M.H. Dickinson, "Visual input to the efferent control system of a fly's "gyroscope"," *Science*, vol. 280, no. 5361, pp. 289–292, 1998.

[7] G. Nalbach, "The halteres of the blowfly *Calliphora*: I. kinematics and dynamics," *Journal of Comparative Physiology A*, vol. 173, pp. 293–300, 1993.

[8] C.P. Taylor, "Contribution of compound eyes and ocelli to steering of locusts in flight: I-II.," *Journal of Experimental Biology*, vol. 93, pp. 1–31, 1981.

[9] T.R. Neumann, "Modeling insect compound eyes: Space-variant spherical vision," in *Proceedings of the 2nd International Workshop on Biologically Motivated Computer Vision BMCV*, T. Poggio H.H. Blthoff, S.-W. Lee and C. Wallraven, Eds., Berlin, Germany, 2002, vol. 2525, pp. 360–367, Springer-Verlag.

[10] A. Fayyazuddin and M.H. Dickinson, "Haltere afferents provide direct, electrotonic input to a steering motor neuron of the blowfly," *Journal of Neuroscience*, vol. 16, no. 16, pp. 5225–5232, 1996.

[11] A. Sherman and M.H. Dickinson, "A comparison of visual and haltere-mediated equilibrium reflexes in the fruit fly *Drosophila melanogaster*," *Journal of Experimental Biology*, vol. 206, pp. 295–302, 2003.

[12] M.H. Dickinson and M.S. Tu, "The function of dipteran flight muscle," *Comparative Biochemistry & Physiology A-Comparative Physiology*, vol. 116, no. 3, pp. 223–238, 1997.

[13] R. Dudley, *The Biomechanics of Insect Flight: Form, Function, Evolution*, Princeton: University Press, 2000.

[14] M.H. Dickinson, F.-O Lehmann, and S.S. Sane, "Wing rotation and the aerodynamic basis of insect flight," *Science*, vol. 284, no. 5422, pp. 1954–1960, 1999.

[15] S.P. Sane and M.H. Dickinson, "The control of flight force by a flapping wing: Lift and drag production," *Journal of Experimental Biology*, vol. 204, no. 15, pp. 2607–2626, 2001.

[16] G.K. Taylor, "Mechanics and aerodynamics of insect flight control," *Biological Review*, vol. 76, no. 4, pp. 449–471, 2001.

[17] L. Tammero and M.H. Dickinson, "The influence of visual landscape on the free flight behavior of the fruit fly *Drosophila melanogaster*," *Journal of Experimental Biology*, vol. 205, pp. 327–343, 2002.

[18] J. Brady, "Flying mate detection and chasing by tsetse flies (*Glossina*)," *Physiological Entomology*, vol. 16, pp. 153–161, 1991.

[19] M. Sitti, D. Campolo, J. Yan, R.S. Fearing, T. Su, D. Taylor, and T. Sands, "Development of PZT and PZN-PT based unimorph actuators for micromechanical flapping mechanisms," in *Proc. of the IEEE International Conference on Robotics and Automation*, Seoul, South Korea, May 2001, pp. 3839–3846.

[20] J. Yan, R. Wood, S. Avandhanula, M. Sitti, and R.S. Fearing, "Towards flapping wing control for a micromechanical flying insect," in *Proc. of the IEEE International Conference on Robotics and Automation*, 2001, vol. 4, pp. 3901–3908.

[21] L. Zhou, J.M. Kahn, and K.S.J. Pister, "Corner-cube reflectors based on structure-assisted assembly for free-space optical communication," *Journal of Microelectromechanical Systems*, vol. 12, no. 3, pp. 233–242, June 2003.

[22] C.P. Ellington, "The aerodynamics of hovering insect flight. I-VI," *Philosophical Transactions of the Royal Society of London B Biological Sciences*, vol. 305, pp. 1–181, 1984.

[23] R. Ramamurti and W.C. Sandberg, "A three-dimensional computational study of the aerodynamic mechanisms of insect flight," *Journal of Experimental Biology*, vol. 205, no. 10, pp. 1507–1518, 2002.

[24] M. Sun and J. Tang, "Lift and power requirements of hovering flight in *Drosophila virilis*," *Journal of Experimental Biology*, vol. 205, no. 10, pp. 2413–2427, 2002.

[25] A.P. Willmott, C.P Ellington, C. van den Berg, and A.L.R Thomas, "Flow visualization and unsteady aerodynamics in the flight of the hawkmoth *Manduca sexta*," *Philosophical Transactions of the Royal Society of London B Biological Sciences*, vol. 352, pp. 303–316, 1997.

[26] X. Deng, L. Schenato, and S.S. Sastry, "Flapping flight for biomimetic robotic insects. Part II: Flight control design," *Submitted to IEEE Transactions on Robotics*.

[27] A.M. Kuethe and C.Y. Chow, *Foundations of Aerodynamics*, John Wiley and Sons, 1986.

[28] Y.C. Fung, *An Introduction to the Theory of Aeroelasticity*, New York, Dover, 1969.

[29] R. M. Murray, Z. Li, and S.S. Sastry, *A Mathematical Introduction to Robotic Manipulation*, CRC Press, 1994.

[30] M.H. Dickinson, ," Personal communication.

[31] S.N. Fry, R. Sayaman, and M. H. Dickinson, "The aerodynamics of free-flight maneuvers in *Drosophila*," *Science*, vol. 300, no. 5618, pp. 495–498, April 2003.

[32] B. Wie, *Space vehicle dynamics and control*, AIAA Educational Series, Reston, VA, 1998.

[33] S. Avadhanula, R.J. Wood, D. Campolo, and R.S. Fearing, "Dynamically tuned design of the MFI thorax," in *Proc. of the IEEE International Conference on Robotics and Automation*, Washington, DC, May 2002, pp. 52–59.

[34] L. Schenato, W.C. Wu, and S.S. Sastry, "Attitude control for a micromechanical flying insect via sensor output feedback," *IEEE Transactions on Robotics and Automation*, vol. 20, pp. 93–106, April 2004.

[35] W.C. Wu, L. Schenato, R.J. Wood, and R.F. Fearing, "Biomimetic sensor suite for flight control of MFI: Design and experimental results," in *Proceeding of IEEE International Conference on Robotics and Automation*, September 2003, pp. 1146–1151.

[36] W.C. Wu, R.J. Wood, and R.F. Fearing, "Halteres for the micromechanical flying insect," in *ICRA*, 2002, pp. 60–65.

[37] R. Hengstenberg, "Mechanosensory control of compensatory head roll during flight in the blowfly *Calliphora erythrocephala*," *Journal of Comparative Physiology A-Sensory Neural & Behavioral Physiology*, vol. 163, pp. 151–165, 1988.

[38] A. Borst and M. Egelhaaf, "Principles of visual motion detection," *Trends in Neuroscience*, vol. 12, pp. 297–306, 1989.

[39] W. Reichardt, "Movement perception in insects," in *Processing of optical data by organisms and machines*, W. Reichardt, Ed., pp. 465–493. Academic, New York, 1969.

[40] R.R. Harrison, *An analog VLSI motion sensor based on the fly visual system*, Ph.D. thesis, California Institute of Technology, Pasadena, May 2000.

[41] W. Reichardt and M. Egelhaaf, "Properties of individual movement detectors as derived from behavioural experiments on the visual system of the fly," *Biological Cybernetics*, vol. 58, no. 5, pp. 287–294, 1988.